Research Square

Preprints are preliminary reports that have not undergone peer review.
They should not be considered conclusive, used to inform clinical practice,
or referenced by the media as validated information.

Ferrocene heteroconjugation of DNA duplex aids Fowler–Nordheim tunnelling

Koji nakano

nakano@cstf.kyushu-u.ac.jp

Kyushu University

Physical Sciences - Article

Keywords:

Posted Date: January 13th, 2026

DOI: https://doi.org/10.21203/rs.3.rs-8010282/v1

License: This work is licensed under a Creative Commons Attribution 4.0 International License.
Read Full License

Additional Declarations: There is **NO** Competing Interest.

Ferrocene heteroconjugation of DNA duplex aids Fowler–Nordheim tunnelling

DNA has emerged as a promising self-assembling material in molecular electronics. Beyond the research on DNA tiles and DNA origami, increasing attention is now being directed towards three-dimensional architectures that may endow electromechanic nanodevices. In this report, we present a method to impart electrical conductivity to DNA: a ferrocene-derivatised psoralen that binds with opposing thymines at T-A/A-T sites, resulting in a covalent cross-link in double-stranded DNA. We found that a thiol-modified, 10-mer DNA formed a 1:1 conjugate, which further self-assembled on Au substrates, allowing for the simultaneous imaging of surface topography and current distribution using conductive atomic force microscopy. The electrical junction thus formed resembles a metal/insulator/metal diode; the current-voltage characteristics were well described using the Fowler–Nordheim tunnelling theory, incorporating an electronic state of psoralen derived from ab initio calculations as the barrier potential. Untreated DNAs and psoralen conjugates lacking the ferrocene moiety exhibited no conductivity. Therefore, a process analogous to dopant incorporation into inorganic semiconductor materials has become feasible for inherently insulating DNA. As no pre-derivatisation of the host DNA is required, any DNA supramolecular structure can be post-processed after synthesis, offering broad versatility. Our findings provide a significant step towards integrating DNA supramolecular chemistry with molecular electronics.

DNA is a promising nanowire material for molecular electronics, where each molecular component functions analogously to conventional electronic parts.[1-3] Over the past 20 years, fluorometric energy transfer experiments have revealed that photoinduced holes and excess electrons within DNA matrices are essential for energy migration.[4] In contrast, DNA charge transport studies[5, 6] integrating metal probe pairs, thus resembling a Schottky diode, have examined the diode behaviour using native DNA but were confined to macroscopic bulk films.[7, 8] Recently, Yoon et al. demonstrated that a two-dimensional DNA lattice with a thickness of only a few nanometres operates effectively as a tunnel diode in a metal/insulator/metal (MIM) configuration.[9] A subsequent study explored a hyperbranched DNA polymer on the order of 50 nm, which, unlike the DNA lattice, behaved as a thermionic diode.[10] However, as in the charge transport pathway, the relatively high LUMO energies of nucleobases pose challenges for efficient device operation.

In the report, we benefit from the use of a redox-functionalized psoralen developed by Nakano et al.[11,12] Psoralen photochemistry enabled covalent incorporation of a ferrocene (Fc) unit with minimal distortion of the B-form helix, forming a 1:1 Fc-psoralen-DNA conjugate for self-assembly (SA). Ab initio calculations estimated a LUMO energy of –4.46 eV for the Fc-psoralen derivative. Conductive atomic force

microscopy (CAFM) with Pt-coated silicon probes (Fig. 1) demonstrated that such conjugation imparts conductivity to normally insulating monolayers, yielding stable *I–V* curves with defined barrier potentials that are consistent with Fowler–Nordheim tunnelling (FNT). The heterogeneous nucleobase-binding molecule can address the efficiency issue in an MIM with functionality analogous to an inorganic semiconductor dopant. Interestingly, probe retraction-recontact cycles produce distinct *I–V* responses, reflecting local structural rearrangements. Non-contact atomic force microscopy (NCAFM) images revealed surface-oriented Fc-psoralen-DNA conjugates at single-molecule resolution, confirming MIM operation at the single-molecule level.

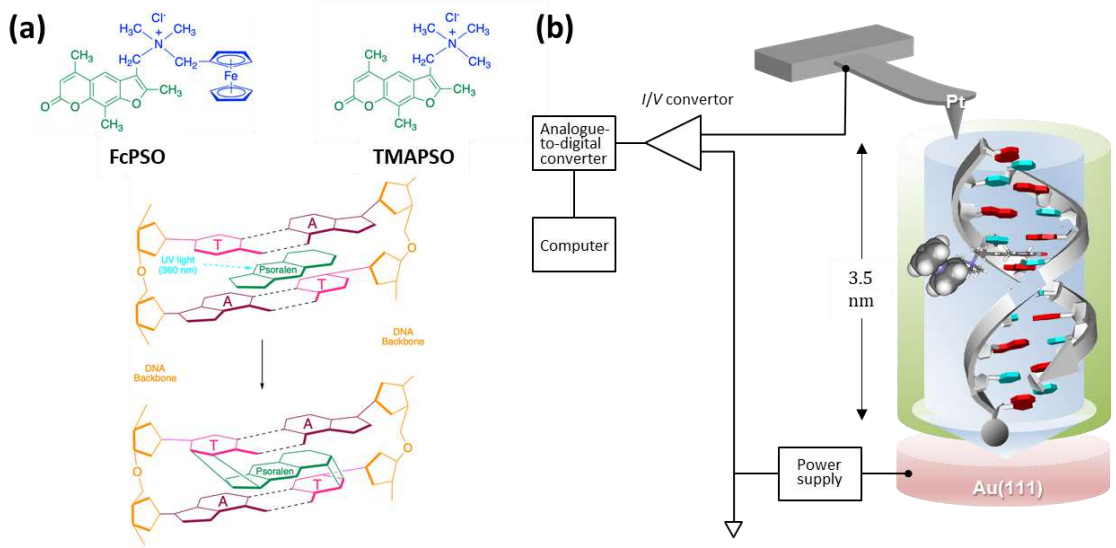


Fig. 1. Illustration of **(a)** DNA conjugate formed by ferrocenylpsoralen (**FcPSO**)

or trimethylammoniopsoralen (**TMAPSO**), and **(b)** *I*/*V* measurement system for conductive atomic force microscopy.

Conductive AFM experiments

Figure 2 summarises the results of CAFM experiments. The development of FcDNA SAs on the Au(111) surface facilitated electrical currents of approximately 1 nA or higher, which was observed across all areas studied. The specific conductivity allowed the SAs to produce current images with features such as surface topography data. Similarly, a bare Au(111) exhibited current magnitudes beyond the maximum measurable by CAFM. However, the current dropped completely below the detection limit after the SAs of native dsDNA developed. Notably, even when the dsDNA was conjugated with psoralen, the resulting SAs did not show any measurable current unless the ferrocene unit was included. These results indicate that the covalently bound ferrocene moiety is critical in electrical conduction across the DNA SAs (*Extended Data Fig. 1*). CAFM was used to further analyse the conductive behaviour of *I–V* responses from the DNA SAs.

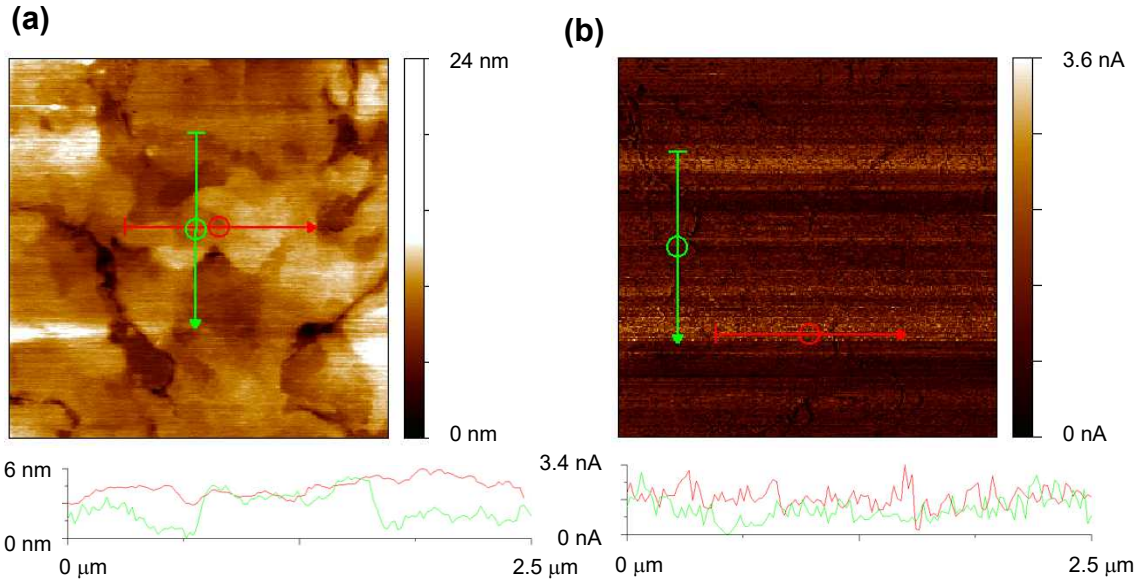


Fig. 2. CAFM results showing simultaneous observation of surface topology and current distribution. **(a)** Topography and **(b)** current image at +10 V for the FcDNA SAs on Au(111), including cross-section profiles with arrow indicators.

Figure 3 shows representative *I–V* curves obtained by CAFM for each Au(111) substrate. For bare Au(111), direct Pt-probe contact caused the current to exceed the instrument limit, and these data are therefore omitted. The self-assembled native dsDNA exhibited no detectable current across the entire bias range (–10 V to +10 V). As noted previously, psoralen conjugation alone did not augment steady-state current unless covalently bound Fc was present. In contrast, FcDNA SAs yielded characteristic *I–V* curves, with forward and reverse currents negligible at low bias voltages but increased

exponentially beyond a specific voltage, consistent with field-activated electron emission. The results demonstrate that FcDNA SAs act as dielectric layers with moderate energy barriers towards the conductive metal terminals. The resulting MIM configuration displayed high reproducible behaviour with nearly invariant *I–V* responses across measurements. During CAFM experiments, the retraction-approach procedure of the CAFM probe, which is required to stabilise surface contact, introduced noticeable variation in the *I–V* curve. Nevertheless, repeated measurements revealed consistent, non-random patterns in these variations, suggesting underlying structural or electronic effects rather than measurement artefacts.

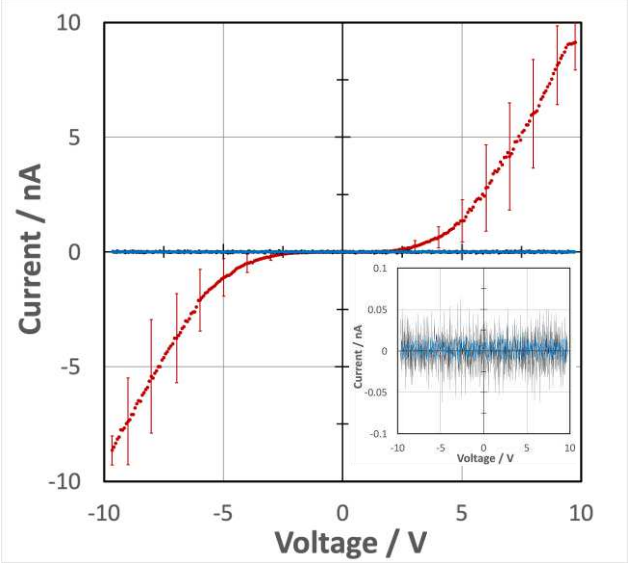


Fig. 3. The results of *I–V* measurements for the Au(111) substrates with dsDNA SAs (blue), TMADNA SAs (black), and FcDNA SAs (red). For FcDNA SAs, the average

currents from four independent measurements are plotted. The inset shows an expanded plot for dsDNA SAs (blue) and TMADNA SAs (black).

Non-contact AFM imaging of DNA SAs

We further probed the same FcDNA SAs/Au(111) substrate using NCAFM to analyse the insulator surface that the CAFM probe contacted. Following the CAFM analysis, the NCAFM image (Fig. 4) revealed that multiple surface objects blanket nearly all atomically flat Au(111) grains. Each object is a single FcDNA molecule, because no such objects were observed on unmodified Au(111). The FcDNA SAs possess shallow regions at specific surface fractions, as indicated by the NCAFM images, which show distinct shapes, either hemispherical or cylindrical. The height data in each pixel of Fig. 4**(b)** were used to prepare the histogram in Fig. 4**(c)**, providing further insight into the surface characteristics. The height is defined as the relative displacement of the lowest pixel in the topographic image. Nonlinear curve fitting subsequently separated this data into three Gaussian peaks. The 0.4 nm first peak accounted for a 12% specific fraction of the surface corresponding to the shallow domains. The peaks at higher frequency had contributions from 1.1 and 0.90 nm, which are attributed to vertically oriented FcDNA (56%) and 35° tilted FcDNA (32%), respectively.[14]

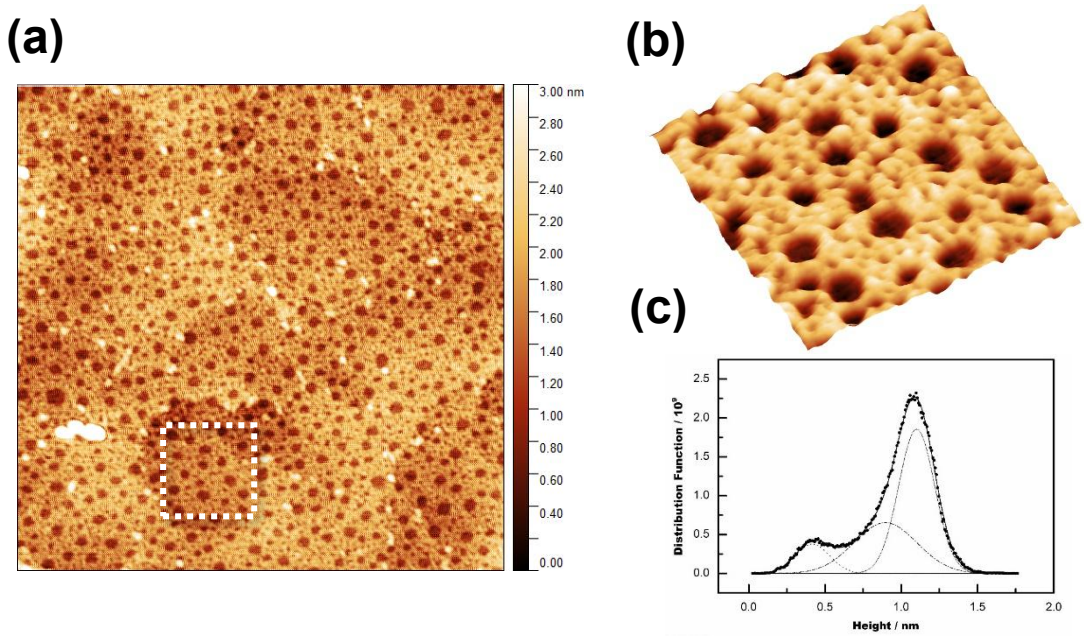


Fig. 4. NCAFM images of **(a)** FcDNA SAs/Au(111) used for CAFM experiments (1 × 1 μm), **(b)** a close-up view of the square area by high-resolution imaging indicated in the 3D representation (200 × 200 nm), and **(c)** a histogram of the surface height for the enlarged image.

These surface nanostructures in the MIM formed the conduction mechanism. As the conductive metal Pt-probe approaches the DNA SA, which acts as an insulator phase, the probe initially contacts the apex of the monolayer to establish an electrical junction. Perpendicular stacks of FcDNA molecules are likely critical, because they form the highest features and occupy the largest fraction of the monolayer area. In contrast, according to the Hertz model[15]—a two-sphere point contact model—the probe contact

area was estimated to be 1.3 nm^2 (*Supplementary information*). This area is smaller than half of the cross-section of dsDNA, indicating that only a single FcDNA molecule participates in electrical conductance. NCAFM revealed that the FcDNA molecules were densely packed in a distorted hexagonal packing lattice. Given that the Pt-probe is much larger than the contact area, a few neighbouring FcDNA molecules may engage simultaneously in the electrical junction. The packing structure thus plays a crucial role in defining an effective contact interface.

Asymmetric tunnelling diode behaviour

Next, ab initio calculations[16] of **FcPSO** provided insights into the electronic properties (*Extended Data Fig. 3*). The results indicated that the LUMO (–4.46 eV) is localised on the psoralen moiety, whereas the HOMO (–8.62 eV) resides on the ferrocene unit. Thus, **FcPSO** functions as an electron acceptor with a moderate barrier potential when paired with a commonly used conducting substrate. Although DNA is an organic material, its relatively high dielectric properties mitigate charge-charge destabilisation. CAFM experiments verified stable *I–V* curves that exhibited field-driven electron emission, which is consistent with the FNT theory.[17] Simmons extended this theory to the characterisation of MIMs.[18, 19] Cowell et al. used this theory to assess the barrier heights

of MIMs where the work function was unknown.[20] The present findings allow construction of an energy band diagram (Fig. 5) with well-defined tunnelling parameters.

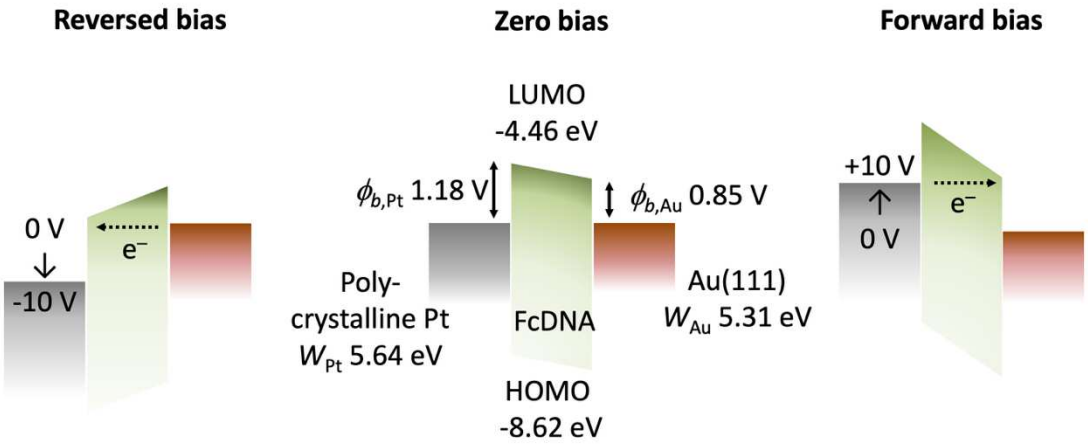


Fig. 5. Illustration of physical layers of the asymmetric tunnelling MIM diode.

In the Pt-tip/FcDNA-SAs/Au(111) MIM, the conduction electrons face non-identical barriers ($\phi_{b,\mathrm{Pt}}$ and $\phi_{b,\mathrm{Au}}$), leading to a different barrier height at zero bias (Fig. 5, centre panel). As the MIM is increasingly biased with either a positive (forward) potential V^+ or a negative (reverse) potential V^-, the direct tunnelling mechanism initially dominates. However, FNT becomes dominant when the bias exceeds the barrier height (Fig. 5, side panels). The FNT describes the forward and reverse currents as given in Equations 1 and 2, respectively (*Supplementary information*). Here, (*Area*) is the

device area, $\phi_{b,\mathrm{Pt}}$ and $\phi_{b,\mathrm{Au}}$ are the heights of the injecting barriers formed between the Pt-probe or Au(111) substrate and FcDNA SAs, respectively, and $\Delta\phi = \phi_{b,\mathrm{Pt}} - \phi_{b,\mathrm{Au}}$. Additionally, *s* is the thickness, and m^* denotes the effective tunnelling mass of an electron in the insulator.

$$I^+ = \frac{(Area)C_1}{\phi_{b,\mathrm{Pt}}} \cdot \frac{(V+\Delta\phi)^2}{s^2} \cdot \exp\left(-C_2\sqrt{m^*}\left(\phi_{b,\mathrm{Pt}}\right)^{\frac{3}{2}}\frac{s}{V+\Delta\phi}\right) \quad (1)$$

$$I^- = \frac{-(Area)C_1}{\phi_{b,\mathrm{Au}}} \cdot \frac{(V+\Delta\phi)^2}{s^2} \cdot \exp\left(-C_2\sqrt{m^*}\left(\phi_{b,\mathrm{Au}}\right)^{\frac{3}{2}}\frac{s}{V+\Delta\phi}\right) \quad (2)$$

C_1 and C_2 are universal constants, as shown in Equations 3 and 4:

$$C_1 = \frac{2.2q^2}{8\pi h} = 3.4 \times 10^{-6} \quad (3)$$

$$C_2 = \frac{23\pi\sqrt{qm_0}}{6h} = 6.9 \times 10^9 \quad (4)$$

The linearised forms of I^+ and I^- may demonstrate a linear relationship when $\log(|I/(V+\Delta\phi)^2|)$ is plotted against $1/(V+\Delta\phi)$. In the forward bias case, the plots produced a straight line across nearly two decades, indicating that FNT dominates the electrical conduction. A simple regression analysis yielded a slope (m^+) of –3.52 and an intercept (b^+) of –9.64, as defined by Equations 5 and 6 (*Extended Data Fig. 2*).

$$m^{+} = \frac{-C_2 s\sqrt{m^*}(\phi_{b,\mathrm{Pt}})^{\frac{3}{2}}}{2.3} \quad (5)$$

$$b^{+} = \log\left(\frac{(Area)C_1}{s^2\phi_{b,\mathrm{Pt}}}\right) \quad (6)$$

Similarly, the reverse current provided the parameters 1.99 and –9.81.

$$m^{-} = \frac{C_2 s\sqrt{m^*}(\phi_{b,\mathrm{Au}})^{\frac{3}{2}}}{2.3} \quad (7)$$

$$b^{-} = \log\left(\frac{(Area)C_1}{s^2\phi_{b,\mathrm{Au}}}\right) \quad (8)$$

We then examined how the FNT parameters we obtained reproduced the experimental *I–V* curves. Since the insulator thickness remained undetermined, we assumed *s* to be 3.5 nm, based on the structural characteristics of dsDNA, which is a standard approximation because of its longitudinal length in molecular models. These considerations yielded values of 0.067 and 0.022 for m^* in the forward and reverse biases, respectively. Importantly, the covalently bound Fc, an electron acceptor, allows dsDNA, essentially an insulator, to exhibit an effective mass for electrons equivalent to that observed in semiconductors.[21] Although we observed a semiconductor-like behaviour, we were unable to reproduce the experimental *I–V* results accurately because the current

values were significantly larger than expected, possibly because of inconsistencies in the electrical contact or measurement setup. In any electrical measurement for a nanometre-sized material, the conductive metal probe often fails to establish electrical contact reproducibly. Therefore, we attributed the discrepancy to the electrical junction not being at the Pt-probe but on the other side, i.e., the FcDNA/Au(111) interface. The alkanethiol linker created this junction with a much smaller footprint than dsDNA, potentially contributing to the discrepancy by leaving most of the surrounding space empty and filled by vacuum, which can affect the electrical measurements. To address the discrepancy between the experimental and theoretical current values, we first identified a predetermined empirical constant. This constant is commonly used in scanning tunnelling microscopy to account for variations in current measurements. We then aimed to correct the experimental current by dividing it by this constant. The relationship between the current and the molecular structure is given by Equation 9:

$$I \propto e^{-\beta n} \tag{9}$$

In this equation, β is the attenuation coefficient of the alkanethiol linker, and n is the number of methylene groups. Typically, a value of $1\,\text{Å}^{-1}$ is used for β, whereas the

molecular length per methylene group is 1.26 Å. Experimentally, we determined the value of β by adjusting it until the FNT equation matched the experimental forward current (Fig. 6**(a)**). This approach was validated as it ensures consistency between theoretical predictions and observed data. We then used this value to calculate the linker chain length based on Equation 9. Using the determined value of β, we calculated the apparent distance to be 1.5 nm, which agreed well with the expected length for the alkyl linker when in an extended, all-trans conformation. However, correction using the same constant did not yield satisfactory results for the negative current, possibly because the Au(111) substrate side was mainly in a vacuum, leading to a more pronounced attenuation effect. Further investigation is required to clarify this point and understand the empirical role of the constant in this context.

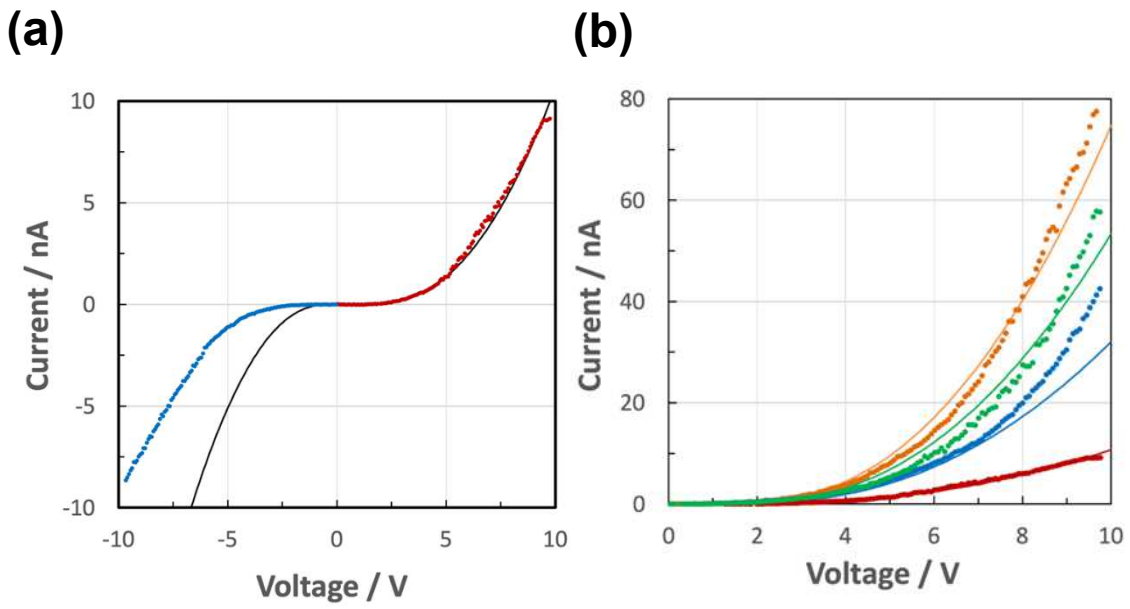


Fig. 6. (a) Comparison of the experimental *I–V* curves with the reproduced data (black line) and **(b)** variation of the experimental *I–V* curves (coloured dots) and comparison with the reproduced *I–V* data. The theoretical data in **(a)**, as shown by the red line, were multiplied by an integer *n* and plotted as solid lines, with $n = 1$ (red), $n = 3$ (blue), $n = 5$ (green), and $n = 7$ (orange).

Possible single dsDNA tunnel diode

In this final section, we examined the retraction of the microscope probe and contact operations during MIM fabrication, which resulted in markedly different *I–V* characteristics (Fig. 6**(b)**). The smallest plot corresponds to the forward current in Fig. 6**(a)** and is shown with the corresponding theoretical curve for comparison. Repeated measurements incorporating probe retraction showed that the *I–V* responses were categorised according to current magnitude, and representative examples from each classification are also displayed. Analysis of these data showed that the linearised FNT plots exhibited weak one-dimensionality, preventing firm quantitative conclusions from being drawn. Nevertheless, scaling the minimum theoretical dataset by an integer factor yielded close agreement with the experimental curve, indicating a quantifiable relationship between the theoretical model and experimental data. This finding supports

the concept that individual FcDNA molecules contribute to the FNT current on a single-molecule basis. The contact area between the Pt-tip and FcDNA is less than half the cross-sectional area of dsDNA, consistent with the molecular packing structure discussed earlier, and impacts the electrical connection. The distorted hexagonal arrangement of FcDNA within the monolayer indicates that several molecules can participate in electrical connection, depending on the exact point of Pt-tip contact. The discrete current classifications observed for positive bias likely correspond to the number of FcDNA molecules engaged in the junction.

Conclusions

Research on DNA nanowires, inspired by advances in molecular electronics technology, has expanded to include novel structures such as gold-coated DNA nanowires,[22] metallic DNA nanowires,[23] and gold nanowires utilising DNA origami structures.[24] Recent developments in DNA nanotechnology have further enabled the construction of various three-dimensional molecular assemblies, which extend the potential applications of DNA nanowires to more diverse nanomechanical devices beyond their original scope.[25-27] However, because native DNA is essentially insulating, its role in nanoelectronic devices remains confined to passive elements such as capacitors. We

have demonstrated that B-type DNA double helices, in which ferrocene is conjugated to thymine bases through psoralen-mediated photochemistry, constitute a novel class of active nanoelectronic materials. This heteroconjugation strategy preserves base pair hydrogen bonding and can be applied to pre-formed double helices at each A-T/T-A site, enabling broad compatibility with supramolecular DNA structures. The direct attachment of ferrocene to thymine pairs introduces an energy level akin to metals, thereby modifying the intrinsic electronic properties of the DNA host. CAFM measurements on Pt-tip/DNA-SAs/Au(111) junctions exhibited *I–V* characteristics typical of a MIM diode, which were accurately reproduced by the FNT model using the embedded ferrocene LUMO (–4.47 eV) as the energy barrier. NCAFM imaging at a single-duplex resolution further indicated that the MIM diode operates at the single-molecule level. Recently, Ishii et al. reported polymer semiconductors whose energy levels are tuned by physical doping of redox-active small molecules.[28] Our approach differs fundamentally from this in that the molecular orbitals of ferrocene are directly integrated into the electronic structure of the host DNA. We believe that this heteroconjugation method functions analogously to dopant introduction in semiconductor engineering, thus establishing a fundamental framework for DNA-based active devices.

Online content

Supplementary information.

References

1 Aviram, A. & Ratner, M. Molecular Rectifiers. *Chemical Physics Letters* **29**, 277-283 (1974). https://doi.org/10.1016/0009-2614(74)85031-1

2 Aradhya, S. & Venkataraman, L. Single-molecule junctions beyond electronic transport. *Nature Nanotechnology* **8**, 399-410 (2013). https://doi.org/10.1038/nnano.2013.91

3 Xiang, D., Wang, X., Jia, C., Lee, T. & Guo, X. Molecular-Scale Electronics: From Concept to Function. *Chemical Reviews* **116**, 4318-4440 (2016). https://doi.org/10.1021/acs.chemrev.5b00680

4 Wagenknecht, H.-A. *Charge transfer in DNA: from mechanism to application*. (Wiley-VCH, 2005).

5 Slinker, J., Muren, N., Renfrew, S. & Barton, J. DNA charge transport over 34 nm. *Nature Chemistry* **3**, 228-233 (2011). https://doi.org/10.1038/nchem.982|10.1038/NCHEM.982

6 Zhuravel, R. *et al.* Backbone charge transport in double-stranded DNA. *Nature Nanotechnology* **15**, 836-840 (2020). https://doi.org/10.1038/s41565-020-0741-2

7 Sönmezoglu, S., Sönmezoglu, Ö., Çankaya, G., Yildirim, A. & Serin, N. Electrical characteristics of DNA-based metal-insulator-semiconductor structures. *Journal of Applied Physics* **107**, 124518 (2010). https://doi.org/10.1063/1.3447985

8 Chan, Z., Ahgilan, A., Sabaratnam, V., Tan, Y. & Periasamy, V. Rectification of DNA films self-assembled in the presence of electric field. *Applied Physics Express* **8**, 047002 (2015) http://doi.org/10.7567/APEX.8.047002

9 Yoon, M. *et al.* Charge Transport in 2D DNA Tunnel Junction Diodes. *Small* **13**, 1703006 (2017). https://doi.org/10.1002/smll.201703006

10 Nakano, K., Sawada, T., Mori, Y., Morita, K. & Ishimatsu, R. Covalent Hyperbranched Polymer Self-Assemblies of Three-Way Junction DNA for Single-Molecule Devices. *Langmuir* **36**, 10166-10174 (2020). https://doi.org/10.1021/acs.langmuir.0c01621

11 Spielmann, H. P., Dwyer, T. J., Hearst, J. E. & Wemmer, D. E. Solution structures of psoralen monoadducted and cross-linked DNA oligomers by NMR spectroscopy and restrained molecular dynamics. *Biochemistry* **34**, 12937-12953 (1995).

12 Nakano, K., Shirakawa, S., Taguchi, S., Maeda, M. Redox-Labeling of DNA by

Photoadduct Conjugate Formation with Ferrocene Derivatized Psoralen. *Analytical Sciences Supplements* **17icas**, i291-i292 (2002). https://doi.org/10.14891/analscisp.17icas.0.i291.0

13 Nakano, K., Katsumi, Y., Soh, N. & Imato, T. An Atomic Force Microscopy Assay of Intercalation Binding, Unwinding, and Elongation of DNA, Using a Water-Soluble Psoralen Derivative as a Covalent Binding Probe Molecule. *Bulletin of the Chemical Society of Japan* **83**, 273-275 (2010). https://doi.org/10.1246/bcsj.20090166

14 Zhou, D., Sinniah, K., Abell, C. & Rayment, T. Use of atomic force microscopy for making addresses in DNA coatings. *Langmuir* **18**, 8278-8281 (2002). https://doi.org/10.1021/la0258547

15 Johnson, K. L. *Contact Mechanics*. (Cambridge University Press,1985).

16 Gaussian 03, Revision E.01, Frisch, M. J. *et al.* Gaussian, Inc., Wallingford CT, 2004.

17 Fowler, R. H. & Nordheim, L. Electron emission in intense electric fields. *Proceedings of the Royal Society of London. Series A, Containing Papers of a Mathematical and Physical Character* **119**, 173-181 (1928). https://doi.org/doi:10.1098/rspa.1928.0091

18 Simmons, J. Generalized Formula for Electric Tunnel Effect Between Similar Electrodes Separated by a Thin Insulating Film. *Journal of Applied Physics* **34**, 1793-1803 (1963). https://doi.org/10.1063/1.1702682

19 Simmons, J. Electric Tunnel Effect Between Dissimilar Electrodes Separated by a Thin Insulating Film. *Journal of Applied Physics* **34**, 2581-2590 (1963). https://doi.org/10.1063/1.1729774

20 Cowell, E., Muir, S., Keszler, D. & Wager, J. Barrier height estimation of asymmetric metal-insulator-metal tunneling diodes. *Journal of Applied Physics* **114**, 213703 (2013). https://doi.org/10.1063/1.4839695

21 Sze, S. M., Li, Y. & Ng, K. K. *Physics of Semiconductor Devices*. (Wiley, 2021).

22 Stern, A. *et al.* Highly Conductive Thin Uniform Gold-Coated DNA Nanowires. *Advanced Materials* **30**, 1800433 (2018). https://doi.org/10.1002/adma.201800433

23 Kondo, J. *et al.* A metallo-DNA nanowire with uninterrupted one-dimensional silver array. *Nature Chemistry* **9**, 956-960 (2017). https://doi.org/10.1038/NCHEM.2808

24 Aryal, B. R. *et al.* Four-Point Probe Electrical Measurements on Templated

Gold Nanowires Formed on Single DNA Origami Tiles. *Langmuir* **34**, 15069-15077 (2018). https://doi.org/10.1021/acs.langmuir.8b02225

25 Jones, M. R., Seeman, N. C. & Mirkin, C. A. Programmable materials and the nature of the DNA bond. *Science*, **347**, 1260901 (2015). http://dx.doi.org/10.1126/science.1260901

26 Hong, F., Zhang, F., Liu, Y. & Yan, H. DNA Origami: Scaffolds for Creating Higher Order Structures. *Chem Rev* **117**, 12584-12640 (2017). https://doi.org/10.1021/acs.chemrev.6b00825

27 Madsen, M. & Gothelf, K. V. Chemistries for DNA Nanotechnology. *Chem Rev* **119**, 6384-6458 (2019). https://doi.org/10.1021/acs.chemrev.8b00570

28 Ishii, M., Yamashita, Y., Watanabe, S., Ariga, K. & Takeya, J. Doping of molecular semiconductors through proton-coupled electron transfer. *Nature* **622**, 285-292 (2023). https://doi.org/10.1038/s41586-023-06504-8

29 Isaacs, S. T., Shen, C.-k. J., Hearst, J. E., Rapoport, H. Synthesis and characterisation of new psoralen derivatives with superior photoreactivity with DNA and RNA. *Biochemistry*, **1977**, 16, 1058–1064. https://doi.org/10.1021/bi00625a005

30 Nečas, D., Klapetek, P. Gwyddion: an open-source software for SPM data

analysis. *Central European Journal of Physics*, **2012**, *10*, 181–188. DOI: 10.2478/s11534-011-0096-2

Methods

Trioxsalen, 2,5,9-trimethylfuro[3,2-g]coumarin, was chloromethylated at the 3-position.[29] Subsequently, the intermediate compound was applied to the quaternisation reaction of *N, N*-dimethylaminomethylferrocene to give a (ferrocenylmethyl)ammonium derivative of psoralen (**FcPSO**) (*Extended Data Fig. 3*). A similar reaction using trimethylamine, which has been examined,[13] produced an inactive control, designated **TMAPSO**. The host dsDNA was prepared by annealing a thiol-modified 10-mer oligodeoxynucleotide, 5'-HS–$(AT)_5$–3', with its complementary strand, 5'–$(AT)_5$–3'. This dsDNA was photochemically reacted with the psoralen derivative to form each 1:1 conjugate (*Extended Data Fig. 4*). These products, FcDNA or TMADNA, were subjected to SA on Au(111) substrates in a manner analogous to that commonly used for native DNA duplexes. AFM measurements were made using a JSPM-4210 scanning probe microscope (JEOL Ltd., Tokyo, Japan). In CAFM, silicone-nitride cantilevers with a Pt surface coating (k = 0.03 N/m, f_0 = 10 kHz, r = 30 nm) were used, which had a GND potential while a differential voltage supply controlled the bias of the Au(111) substrate.

The instrument was equipped with an *I–V* converter, utilising an op-amp to detect the current. The sample environment was maintained in a vacuum using a turbo molecular pump (approximately 10^{-4} Pa). In the case of the *I–V* measurement, the bias voltage was scanned from +10 V to –10 V in 16 milliseconds, and the collected data were averaged over 10 successive scans. The instrument was operated in the frequency modulation detection mode under vacuum conditions for NCAFM imaging. Silicon cantilevers (k = 14.0 N/m, f_0 = 315 kHz) were used for the experiments. Standard image processing filters reduced the noise in the raw data, which was provided by Gwyddion data visualisation and analysis software.[30]

Data availability

Acknowledgements

Author contribution

Competing interests

The authors declare no competing interests.

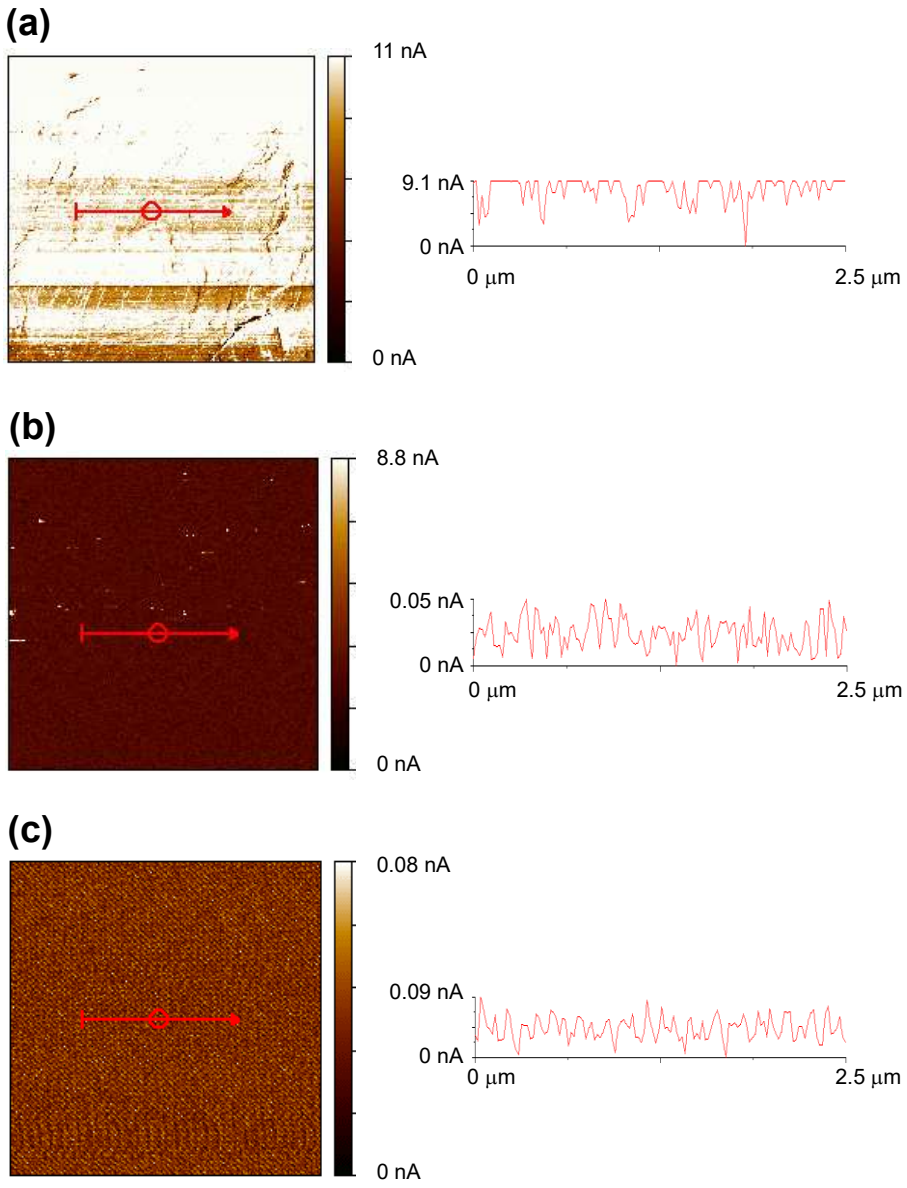
Additional information

Supplementary Information

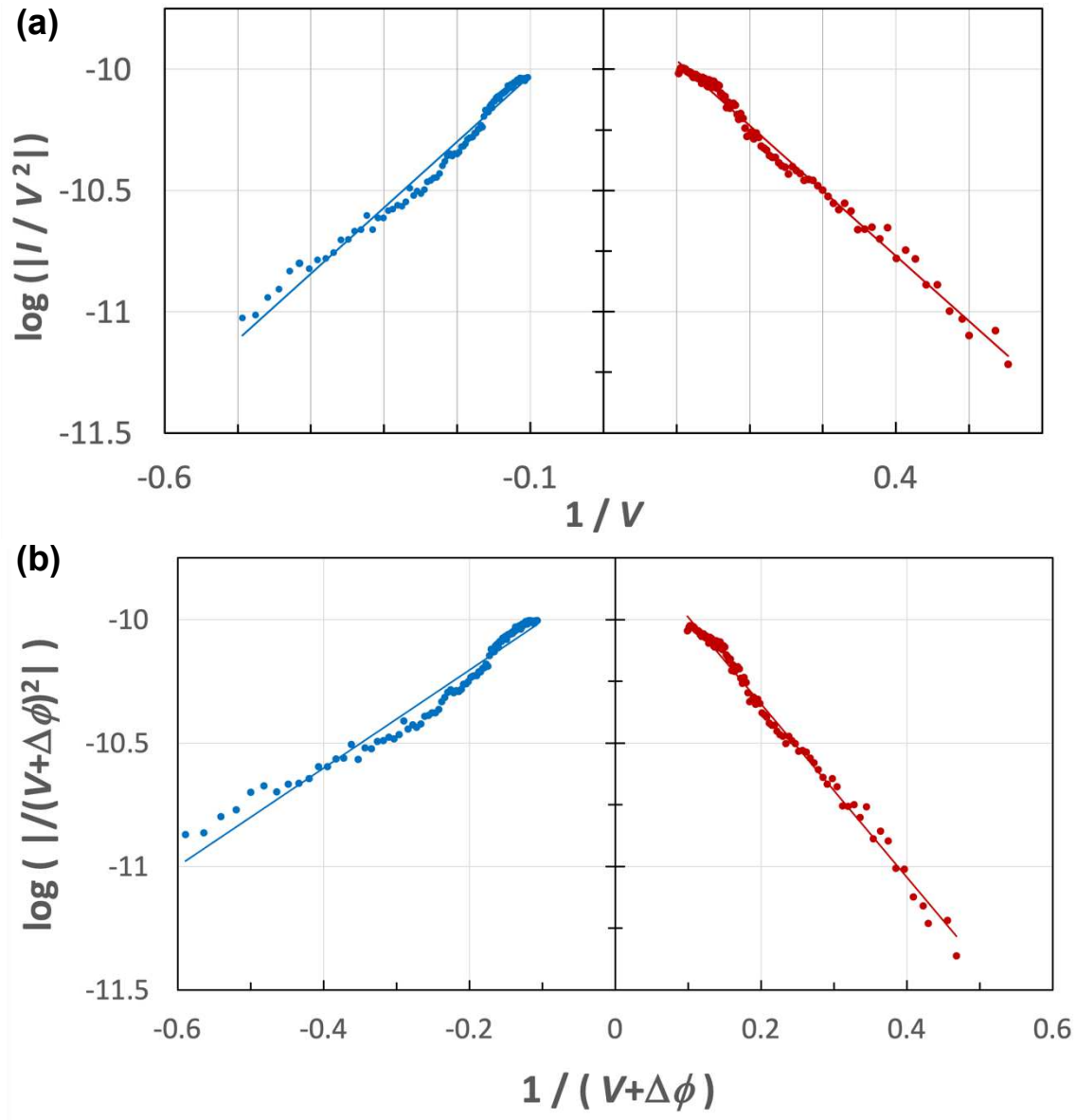
Detailed procedures for synthesising **FcPSO** and the dsDNA conjugate, as well as the DNA SA protocols with the AFM setups. The material also includes an analysis method for *I-V* curves based on the FNT mechanism employed in MIM studies, together with contact area estimation using the equation by Hertz.

Correspondence should be addressed to Koji Nakano.

EXTENDED DATAs

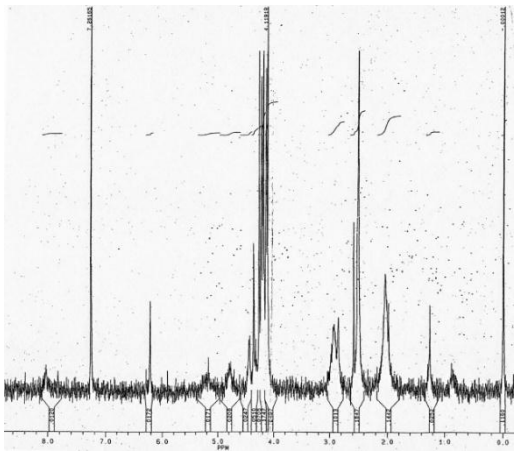


Extended Data Fig. 1. CAFM current images and the cross-section profile with the arrow indicators for **(a)** bare Au(111) at +1.0 V, **(b)** dsDNA SAs on Au(111) at +1.0 V, and **(c)** TMADNA SAs on Au(111) at +8.0 V. The observed area was 5 × 5 μm.

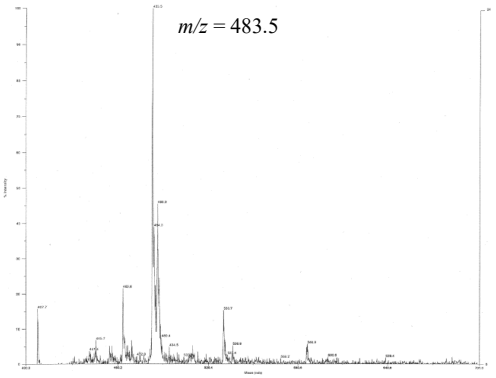


Extended Data Fig. 2. Fowler-Nordheim plots of **(a)** $\log(|I/V^2|)$ against $1/V$, and **(b)** $\log(|I/(V+\Delta\phi)^2|)$ against $1/(V+\Delta\phi)$.

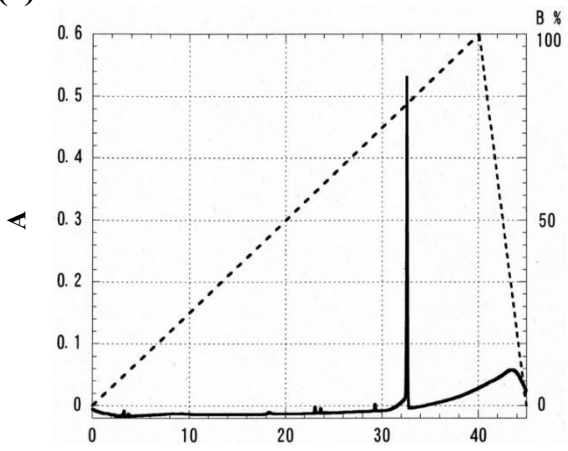
(a)



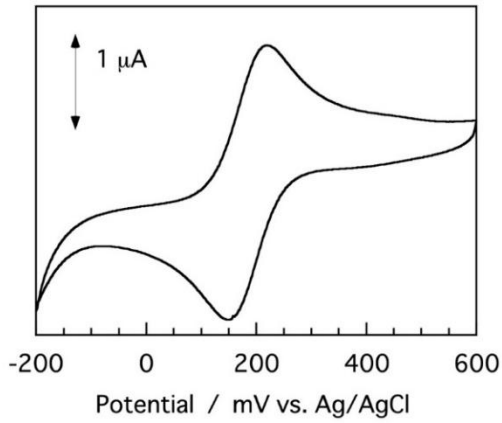
(b)


m/z = 483.5

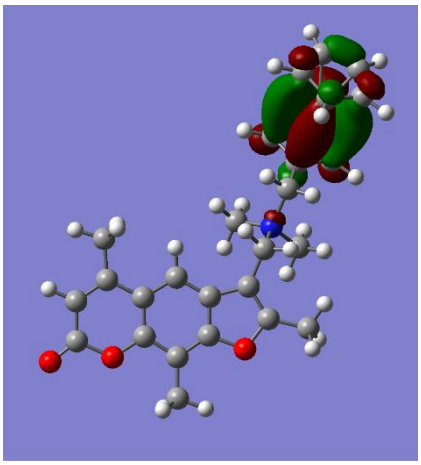
(c)

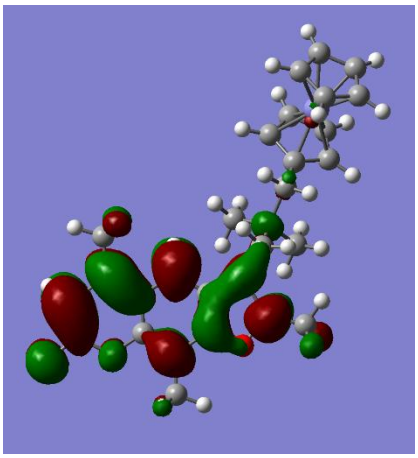

A
B %
0.6
0.5
0.4
0.3
0.2
0.1
0
100
50
0
0
10
20
30
40
Retention time / min

(d)

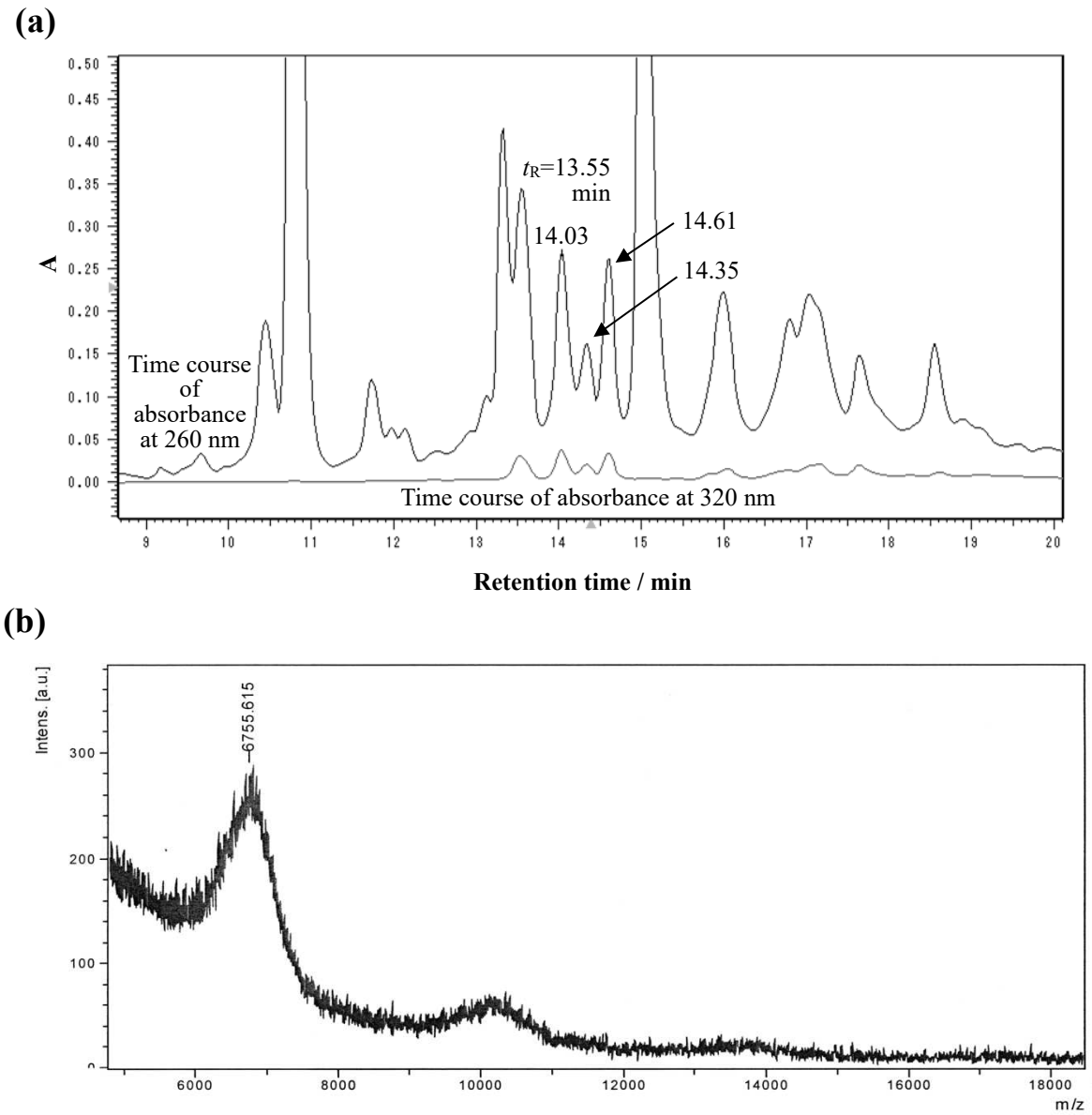

1 μA
-200
0
200
400
600
Potential / mV vs. Ag/AgCl

(e)





Extended Data Fig. 3. (**a**) ^{1}H-NMR, (**b**) MALDI-MS, (**c**) HPLC, (**d**) cyclic voltammogram, and **(e)** graphical representations of HOMO (left panel, −8.62 eV) and LUMO (right panel, −4.46 eV) for **FcPSO**. In voltammetric measurements, a one-chamber cell with a three-electrode configuration, equipped with an Au disk (working electrode, ϕ1.6 mm), a Pt wire (counter electrode), and an Ag/AgCl reference electrode, was used. The electrolyte solution was 0.2 mM **FcPSO** containing 20 mM KCl. A scan rate of 25 mV/s was used, and the temperature was maintained at 25 °C. Ab initio optimizations were performed using the B3LYP method with the LanL2DZ basis set, as implemented in Gaussian 03.



Extended Data Fig. 4. (a) A representative chromatogram for the reaction product and **(b)** MALDI-TOF-MS chart for the fraction at t_R 14.35 min. HPLC separations were made on a C18 silica column (ϕ4 × 250 mm) with a linear gradient condition from 10% acetonitrile to 40% acetonitrile in 30 min. For MS analyses, 3-hydroxy picolinic acid was used as the ionization matrix.

Supplementary Files

This is a list of supplementary files associated with this preprint. Click to download.

- nakanokojisupportinginfo.docx